designed a sample to minimize such a gradient and to maximize uniformity in parameter values across the whole section. It presents a central region where the gradient almost vanishes. The current crowding at the borders, with associated localized lasing, still exists. All other characteristics of the sample remain unchanged with respect to the first one. We repeat the experiments with the new sample, and we observe (Fig. 4a) that the homogeneous state can cover most of the diameter of the VCSEL; this occurs over an appreciable range of frequencies of the external field. A boundary is still observable between a pattern and the homogeneous state, on the left side of the sample. By injecting the writing beam inside the homogeneous state, we can generate a CS that remains when the writing beam is removed. We then apply this beam in a different location without changing any parameter value, and a second spot is generated. This spot will also persist after removal of the writing beam. We reach, then, the situation in which two CSs exist. Changing the phase of the writing beam and re-injecting it successively at the location of each spot, we erase each spot in an independent way. The full series is displayed in Fig. 4. In the experiment, the position of the CS can be changed by adding a weak gaussian beam (in phase with the holding beam and with a smaller waist) in a location lying up to three CS diameters off the soliton peak. After removal of this additional gaussian beam, the CS comes back to one of the previous positions.

The theoretical analyses and numerical simulations had the following features, yielding a consistent interpretation on the observed behaviour of CSs. When simulating the switch-on of a CS in the sample with small resonance gradient ($\nabla\theta$), the CS follows $\nabla\theta$, drifting leftwards until it merges with the pattern. The small intensity gradient of the gaussian holding beam alone is unable to counterbalance the drift. When a stochastic process simulating the sample roughness is accounted for, the CS moves to a location where it remains fixed. The conditions for such 'trapping' depend on the balance between the local resonance and $\nabla\theta$. The number and distribution of such 'trapping sites', related to the imperfections of the device, are interspersed densely enough to allow for a large number of stable CS locations throughout the sample. This effect of layer-related roughness is rather new to investigations[24]: it does not prevent CS motion under the influence of additional field gradients, so that CSs can be manipulated exactly as in the experiment. In particular, the CS drift can be governed by injecting a second gaussian beam with waist smaller than that of the holding beam, but larger than the CS radius. When this beam is positioned close to where the CS has been turned on, it attracts the CS towards its maximum, and traps it in a location where the pull induced by $\nabla\theta$ is balanced by the intensity gradient; this occurs in a range approximately on the order of the gaussian waist, in agreement with the experiment.

Using CSs, we have realized a monolithic two-bit all-optical information processor: we consider that these results open a possible way to developing a practical device. The future development of our results requires an increase in the number of CSs that can be simultaneously present, and also a way of inducing controllable motion of CSs. To achieve these goals, it will be necessary to introduce appropriate spatial modulations in the holding beam, and to further improve the homogeneity of the sample in the transverse plane. □

Received 5 June; accepted 1 August 2002; doi:10.1038/nature01049.

1. McDonald, G. S. & Firth, W. J. Switching dynamics of spatial solitary wave pixels. *J. Opt. Soc. Am. B* **10,** 1081–1089 (1993).
2. Brambilla, M., Lugiato, L. A. & Stefani, M. Interaction and control of optical localized structures. *Europhys. Lett.* **34,** 109–114 (1996).
3. Firth, W. J. & Scroggie, A. J. Optical bullet holes: robust controllable localized states of a nonlinear cavity. *Phys. Rev. Lett.* **76,** 1623–1626 (1996).
4. McLaughlin, D. W., Moloney, J. V. & Newell, A. C. Solitary waves as fixed points of infinite-dimensional maps in an optical bistable ring cavity. *Phys. Rev. Lett.* **51,** 75–78 (1983).
5. Rosanov, N. N. & Khodova, G. V. Autosolitons in bistable interferometers. *Opt. Spectrosc.* **65,** 449–450 (1988).
6. McDonald, G. S. & Firth, W. J. Spatial solitary wave optical memory. *J. Opt. Soc. Am. B* **7,** 1328–1335 (1990).
7. Tlidi, M., Mandel, P. & Lefever, R. Localized structures and localized patterns in optical bistability. *Phys. Rev. Lett.* **73,** 640–643 (1994).
8. Taranenko, V. B., Staliunas, K. & Weiss, C. O. Spatial soliton laser: localized structures in a laser with a saturable absorber in a self-imaging resonator. *Phys. Rev. A.* **56,** 1582–1591 (1997).
9. Saffman, M., Montgomery, D. & Anderson, D. Z. Collapse of a transverse-mode continuum in a self-imaging photorefractively pumped ring resonator. *Opt. Lett.* **19,** 518–520 (1994).
10. Weiss, C. O., Vaupel, M., Staliunas, K., Slekys, G. & Taranenko, V. B. Solitons and vortices in lasers. *Appl. Phys. B* **68,** 151–168 (1999).
11. Schreiber, A., Thuering, B., Kreuzer, M. & Tschudi, T. Experimental investigation of solitary structures in a nonlinear optical feedback system. *Opt. Commun.* **136,** 415–418 (1997).
12. Ramazza, P. L., Ducci, S., Boccaletti, S. & Arecchi, F. T. Localized versus delocalized patterns in a nonlinear optical interferometer. *J. Opt. B* **2,** 399–405 (2000).
13. Schaepers, B., Feldmann, M., Ackemann, T. & Lange, W. Interaction of localized structures in an optical pattern-forming system. *Phys. Rev. Lett.* **85,** 748–751 (2000).
14. Brambilla, M., Lugiato, L. A., Prati, F., Spinelli, L. & Firth, W. J. Spatial soliton pixels in semiconductor devices. *Phys. Rev. Lett.* **79,** 2042–2045 (1997).
15. Michaelis, D., Peschel, U. & Lederer, F. Multistable localized structures and superlattices in semiconductor optical resonators. *Phys. Rev. A* **56,** R3366–R3369 (1997).
16. Spinelli, L., Tissoni, G., Brambilla, M., Prati, F. & Lugiato, L. A. Spatial solitons in semiconductor microcavities. *Phys. Rev. A* **58,** 2542–2559 (1998).
17. Spinelli, L., Tissoni, G., Tarenghi, M. & Brambilla, M. First principle theory for cavity solitons in semiconductor microresonators. *Eur. Phys. J. D* **15,** 257–266 (2001).
18. Taranenko, V. B., Ganne, I., Kuszelewicz, R. & Weiss, C. O. Patterns and localized structures in bistable semiconductor resonators. *Phys. Rev. A* **61,** 063818-5 (2000).
19. Taranenko, V. B., Ganne, I., Kuszelewicz, R. & Weiss, C. O. Spatial solitons in a semiconductor microresonator. *Appl. Phys. B* **72,** 377–380 (2001).
20. Ackemann, T. *et al.* Spatial structure of broad area vertical-cavity regenerative amplifiers. *Opt. Lett.* **25,** 814–816 (2000).
21. Lugiato, L. A., Brambilla, M. & Gatti, A. *Advances in Atomic, Molecular and Optical Physics* (eds Bederson, B. and Walther, H.) **Vol. 40** 229–306 (Academic, Boston, 1998).
22. Thual, O. & Fauve, S. Localized structures generated by subcritical instabilities. *J. Phys.* **49,** 1829–1923 (1988).
23. Grabherr, M. *et al.* Bottom-emitting VCSEL's for high-CW optical output power. *IEEE Photon. Tech. Lett.* **10,** 1061–1063 (1998).
24. Fedorov, S. *et al.* Effects of spatial inhomogeneities on the dynamics of cavity solitons in quadratically nonlinear media. *Phys. Rev. E* **64,** 036610-8 (2001).

Acknowledgements We thank F. Capasso, P. Coullet, W. J. Firth and R. Kuszelewicz for discussions. This work was performed in the framework of the ESPRIT project PIANOS and the PRIN project 'Formazione e controllo di solitoni di cavità in microrisonatori a semiconduttore' of the Italian Ministry of University and Research, the contract ACI Photonique of the Ministere de l'Education et la Recherche de France, and the Project TIC99-0645-C05-02 of the Ministerio de Educación y Cultura, Spain.

Competing interests statement The authors declare that they have no competing financial interests.

Correspondence and requests for materials should be addressed to L.A.L. (e-mail: Luigi.Lugiato@uninsubria.it).

Stacking of conical molecules with a fullerene apex into polar columns in crystals and liquid crystals

Masaya Sawamura*‡, Kenji Kawai*, Yutaka Matsuo*, Kiyoshi Kanie†, Takashi Kato† & Eiichi Nakamura*

** Department of Chemistry, The University of Tokyo, Hongo, Bunkyo-ku, Tokyo 113-0033, Japan*
† Department of Chemistry and Biotechnology, School of Engineering, The University of Tokyo, Hongo, Bunkyo-ku, Tokyo 113-8656, Japan

Polar liquid crystalline materials can be used in optical and electronic applications, and recent interest has turned to formation strategies that exploit the shape of polar molecules and their interactions to direct molecular alignment[1,2]. For example, banana-shaped molecules align their molecular bent within smectic layers[3], whereas conical molecules should form polar

‡ Present address: Department of Chemistry, Hokkaido University, Kita-ku, Sapporo 060-0810, Japan.

columnar assemblies[4–9]. However, the flatness of the conical molecules used until now[4–6,9] and their ability to flip[7,8] have limited the success of this approach to making polar liquid crystalline materials. Here we show that the attachment of five aromatic groups to one pentagon of a C_{60} fullerene molecule yields deeply conical molecules that stack into polar columnar assemblies. The stacking is driven by attractive interactions between the spherical fullerene moiety and the hollow cone formed by the five aromatic side groups of a neighbouring molecule in the same column. This packing pattern is maintained when we extend the aromatic groups by attaching flexible aliphatic chains, which yields compounds with thermotropic and lyotropic liquid crystalline properties. In contrast, the previously reported fullerene-containing liquid crystals[10–17] all exhibit thermotropic properties only, and none of them contains the fullerene moiety as a functional part of its mesogen units. Our design strategy should be applicable to other molecules and yield a range of new polar liquid crystalline materials.

The chemical nature of side groups can tune the assembly of fullerene derivatives into a range of different nanostructures[18]. In our molecular design, which builds on the C_5 symmetry of the C_{60}, we attach five aromatic groups to form a conical cavity with chemical affinity for C_{60} (Fig. 1a). The synthesis involves covalent attachment of five biphenyl groups around one pentagon of C_{60}, using an organocopper-based strategy[19] that produces the pentakis(biphenyl)fullerene **1** on a 10-g scale in 99% isolated yield. The synthesis of molecules with a deep conical structure and flexible side chains started with the addition of five phenol groups to one pentagon, followed by coupling with a benzoate group bearing two long aliphatic side chains. With this modification, the molecule acquires a deep cavity with an aromatic interior at the bottom (red/blue, Fig. 1b) and an aliphatic periphery at the top (grey, Fig. 1c). This design should favour columnar stacking of the molecules into one-dimensional arrays (Fig. 1d): the low affinity of the aliphatic side chains to C_{60} provides a chemical driving force for microphase segregation[2,20]. We note that C_{60} is highly soluble in aromatic hydrocarbons while insoluble in saturated hydrocarbons[21].

The molecules **2–5** bearing hydrocarbon side chains were synthesized in three steps: five-hold addition of 4-(THPO)C_6H_4MgBr (where THP is a tetrahydropyranyl protective group) to C_{60} in the presence of CuBr·Me_2S and acid hydrolysis of the THP group afforded (4-HOC_6H_4)$_5C_{60}$H in 92% yield, followed by acylation of the resulting five phenolic groups with an appropriate acid chloride afforded **2–5** in about 60% overall yield on a multigram scale. Compounds were purified with gel permeation chromatography to analytically pure quality and used for the experiments.

Single crystals of **1** were grown in a mixture of chlorobenzene and diethyl ether. The crystal belongs to the orthorhombic crystal system and the space group of *P*bca. A unit cell comprises four pairs of two molecules stacked in a head-to-tail manner, and infinite translation of the unit cell along the A axis yields one-dimensional arrays of stacked molecules (Fig. 2a). The stacking period of the molecules within a column is 11.1 Å, which includes a small void between neighbouring molecules in the same column. The columns are packed in a hexagonal manner (Fig. 2b). The packing is slightly distorted: The shorter intercolumnar distance (a_{hex}) is 14.2 Å

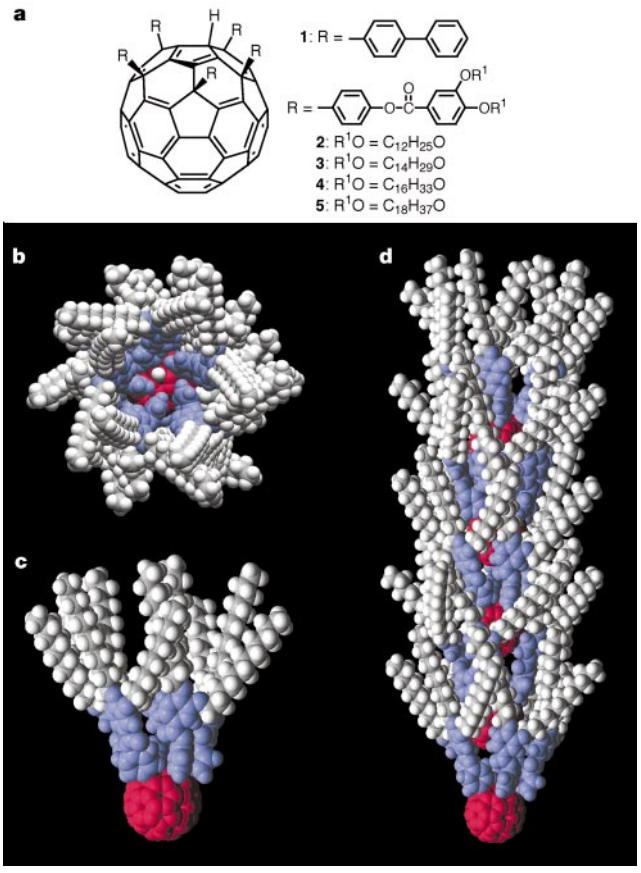

Figure 1 Fullerene derivatives with deeply conical structures. **a**, Chemical formulae of **1**–**5**. **b**, Top view of **2**. Colour code: red, fullerene core; blue, aromatic groups, and grey, alkyl chains. **c**, Side view of **2**. **d**, A stack of five molecules of **2** (based on molecular mechanics calculations and on the SAXD data described in the text).

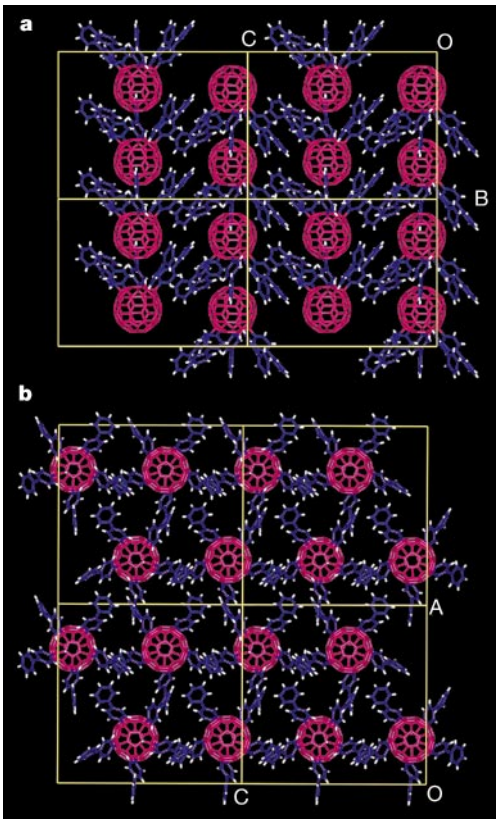

Figure 2 Crystal packing of biphenyl compound **1**. **a**, View from A axis and **b**, from B axis. For clarity, chlorobenzene and diethyl ether molecules are omitted and only a single layer of the molecules is shown. Crystal data for **1**·(C_6H_5Cl)·(Et_2O): $C_{130}H_{61}Cl_1O_1$, orthorhombic space group *P*bca (number 61), $a = 27.7100(9)$ Å, $b = 22.1850(18)$ Å, $c = 28.456(2)$ Å, $V = 17493(2)$ Å^3, $Z = 8$, $T = 213(2)$ K (standard deviation in parentheses), MacScience DIP2030 diffractometer, Mo_{K_α} radiation ($\lambda = 0.71073$). The full-matrix least-square refinement with 15,517 reflections and 1,191 parameters converged to *R*1 factor = 0.1249, w*R*2 factor = 0.3481, and goodness of fit = 1.367.

(Fig. 3c) and the longer one is 17.2 Å. The fullerene core of **1** sits in the cavity created by the five biphenyl groups of the next molecule in the column. Each column is oriented in a direction opposite to the neighbouring columns, with the fullerene cores forming layers perpendicular to the column axes owing to intercolumnar biphenyl-CH/biphenyl-π interactions.

Systems containing fullerenes can exhibit liquid crystalline behaviour, but are usually thermotropic liquid crystals[10–15]. In contrast, compounds **2**–**5** exhibit both thermotropic and lyotropic liquid crystalline properties. We find that these compounds display thermotropic hexagonal columnar phases up to temperatures around 140 °C (Fig. 3a). As the side chain increases in **2**–**5** from 12 carbons to 18, the enthalpy change of the liquid crystal-isotropic transition decreases from 21.0 to 5.0 kJ mol^{-1} whereas the glassy to liquid crystal transition temperature increases monotonously from −47 °C to −7 °C.

The small-angle X-ray diffraction (SAXD) spectrum of **2** at 60 °C shows a sharp reflection with a *d*-spacing of 31.4 Å (100), and smaller peaks associated with *d*-spacings of 16.8 (110), 15.6 (200) and 14.3 Å (001) (Fig. 4a and b). The first three peaks correspond to the reflections of a hexagonal columnar structure (reciprocal *d*-spacing of 1:$\sqrt{3}$:2) and the last peak to the stacking period within the column. In a wide-angle X-ray diffraction pattern (see Supplementary Information), a broad peak centred at 4.5 Å is seen. Its position and width are typical for molten aliphatic moieties. The intercolumnar spacing a_{hex} is 35.3 Å (Fig. 3d), which is more than twice as large as that observed in the crystals of **1** (14.2–17.2 Å, Fig. 3c). Neither the angles nor the intensities of the reflections—*d*(100), (110), (200) and (001)—change (within ± 0.6%) at temperatures between 60 and 140 °C (Fig. 4a). The measured stacking period (14.3 Å) and the intercolumnar spacing (35.3 Å) provide strong evidence of head-to-tail stacking of **2**, which is consistent with molecular mechanics modelling (MM2*-optimized) of the stack structure (Fig. 1d).

Lyotropic mesophases form for a mixture of **2** and dodecane (Fig. 3b). At relatively small **2**/dodecane ratios (w/w), a nematic columnar phase forms. The SAXD data (Fig. 4c) at a 1:1 ratio of **2** and dodecane indicate an intercolumnar distance of about 56.3 Å (at 100 °C). In fact, the SAXD spectra at 60 and 80 °C for the lyotropic hexagonal columnar phase (Fig. 4c and d) are similar to the spectra of the thermotropic mesophase (Fig. 4a and b). Differences are the larger intercolumnar distance (39.8 Å as opposed to 35.3 Å, Fig. 3d) and the appearance of a rather sharp and strong (001) reflection corresponding to an intracolumnar repetition period of 17.5 Å (as opposed to the 14.3 Å period seen in the thermotropic liquid crystal). The relatively strong (001) reflection suggests significant modulation of the electron density along the columns as well as good positional correlation along the column long axis.

Previous fullerene-containing mesogens were built by connecting fullerene molecules to an inherently mesogenic unit[10–15], whereas the present design of the mesogen uses the molecular symmetry of the C_{60} to form anisotropic 'nano-shuttlecocks' that stack into a one-dimensional columnar supramolecular structure. This design

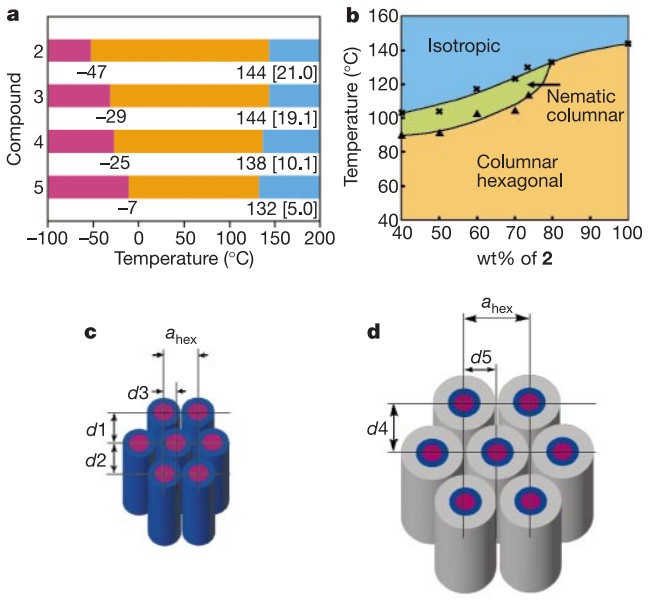

Figure 3 Crystalline and liquid crystalline properties and structures of **1**–**5**. **a**, Thermotropic phase behaviour of **2**–**5**. Pink, glassy phase; orange, liquid crystalline phase; light blue, isotropic phase. Temperatures are in °C, and transition enthalpies in kJ mol^{-1} in brackets. **b**, Lyotropic phase behaviour of a mixture of **2** with various amounts of dodecane. **c**, Schematic of the crystal packing of **1**; $d1 = 13.86$ Å, $d2 = 13.85$ Å, $d3 = 4.5$ Å, $a_{hex} = 14.2$ Å, stacking period is 11.1 Å (the data set refers to the shortest a_{hex} and the related parameters in this distorted hexagonal packing). **d**, Schematic of the column packing of liquid crystalline phases of **2**. For thermotropic liquid crystals of **2** at 60 °C: $d4 = 31.4$ Å, $d5 = 16.8$ Å, $a_{hex} = 35.3$ Å, stacking period is 14.3 Å. For lyotropic liquid crystals of a 50:50 mixture of **2** and dodecane at 60 °C: $d4 = 34.4$ Å, $d5 = 19.9$ Å, $a_{hex} = 39.8$ Å, stacking period is 17.5 Å. Thermal and liquid crystalline properties were determined by differential scanning calorimetry (DSC) measurements on a Mettler DSC30 system and optical observation with an Olympus BX51 microscope equipped with a Mettler FP82-HT hot stage. The liquid crystalline to isotropic transition temperature was taken at the maximum of the endothermic peak in the DSC chart on the second heating run at the rate of 20 °C min^{-1}. The glass transition temperature was read at the midpoint of the change in the heat capacity.

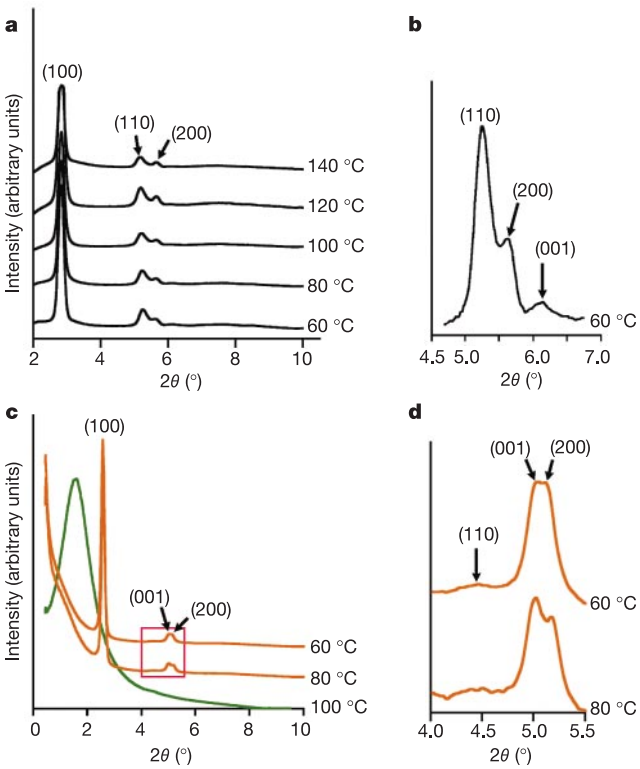

Figure 4 SAXD patterns of liquid crystals of **2**–**5**. **a**, The SAXD spectra of thermotropic liquid crystal of **2** at various temperatures. **b**, A more detailed view of the 4.5–7-degree region at 60 °C. **c**, The SAXD spectra of lyotropic liquid crystal of a 50:50 mixture of **2** and dodecane at 60–100 °C. The colour codes correspond to those used in Fig. 3b. The pink box region is enlarged and shown in **d**. **d**, A more detailed view of the 4–5.5-degree region at 60 and 80 °C. The SAXD profiles were recorded on a Rigaku small-angle X-ray scattering analyser by confocal multilayer mirror.

strategy should be applicable to a range of other molecules and materials. In our system, the driving force for the stacking is the aromatic/fullerene interaction in the concave cavity, and the incompatibility of the fullerene/aromatic system and the aliphatic side chain/solvent system[2,20]. The $R_5C_{60}H$ core structure used here exhibits electron absorption spectra and electrochemical properties similar to those of its C_{60} parent[22], and we therefore expect that the liquid crystalline material described here might exhibit interesting optical and electrochemical properties. Moreover, the species $R_5C_{60}H$ can be transformed into a variety of stable η^5-metal complexes $R_5C_{60}M$ (where M is metal)[23], such as a redox-active ferrocene/fullerene hybrids[24]; this property might allow metal-doping of the fullerene-based crystals and liquid crystals and thus expand the scope of this type of material[25]. □

Received 1 July; accepted 30 August 2002; doi:10.1038/nature01110.

1. Guillon, D. Molecular engineering for ferroelectricity in liquid crystals. *Adv. Chem. Phys.* **113,** 1–49 (2000).
2. Kato, T. Self-assembly of phase-segregated liquid crystal structures. *Science* **295,** 2414–2418 (2002).
3. Niori, T., Sekine, T., Watanabe, J., Furukawa, T. & Takezoe, H. Distinct ferroelectric smectic liquid crystals consisting of banana shaped achiral molecules. *J. Mater. Chem.* **6,** 1231–1233 (1996).
4. Cometti, G., Dalcanale, E., Du Vosel, A. & Levelut, A.-M. New bowl-shaped columnar liquid crystals. *J. Chem. Soc. Chem. Commun.* 163–165 (1990).
5. Xu, B. & Swager, T. M. Rigid bowlic liquid crystals based on tungsten-oxo calix[4]arenes: host-guest effects and head-to-tail organization. *J. Am. Chem. Soc.* **115,** 1159–1160 (1993).
6. Komori, T. & Shinkai, S. Novel columnar liquid crystals designed from cone-shaped calix[4]arenes. The rigid bowl is essential for the formation of the liquid crystal phase. *Chem. Lett.* 1455–1458 (1993).
7. Malthête, J. & Collet, A. Liquid crystals with a cone-shaped cyclotriveratrylene core. *Nouv. J. Chim.* **9,** 151–153 (1985).
8. Malthête, J. & Collet, A. Inversion of the cyclotribenzylene cone in a columnar mesophase: a potential way to ferroelectric materials. *J. Am. Chem. Soc.* **109,** 7544–7545 (1987).
9. Kang, S. H. *et al.* Novel columnar mesogen with octupolar optical nonlinearities: synthesis, mesogenic behaviour and multiphoton-fluorescence-free hyperpolarizabilities of subphthalocyanines with long aliphatic chains. *Chem. Commun.* 1661–1662 (1999).
10. Chuard, T. & Deschenaux, R. First fullerene[60]-containing thermotropic liquid crystal. *Helv. Chim. Acta* **79,** 736–741 (1996).
11. Chuard, T., Deschenaux, R., Hirsch, A. & Schönberger, H. A liquid-crystalline hexa-adduct of [60]fullerene. *Chem. Commun.* 2103–2104 (1999).
12. Tirelli, N., Cardullo, F., Habicher, T., Suter, U. W. & Diederich, F. Thermotropic behaviour of covalent fullerene adducts displaying 4-cyano-4'-oxybiphenyl mesogens. *J. Chem. Soc. Perkin Trans.* **2,** 193–198 (2000).
13. Felder, D., Heinrich, B., Guillon, D., Nicoud, J.-F. & Nierengarten, J.-F. A liquid crystalline supramolecular complex of C_{60} with a cyclotriveratrylene derivative. *Chem. Eur. J.* **6,** 3501–3507 (2000).
14. Dardel, B., Guillon, D., Heinrich, B. & Deschenaux, R. Fullerene-containing liquid-crystalline dendrimers. *J. Mater. Chem.* **11,** 2814–2831 (2001).
15. Chuard, T. & Deschenaux, R. Design, mesomorphic properties, and supramolecular organization of [60]fullerene-containing thermotropic liquid crystals. *J. Mater. Chem.* **12,** 1944–1951 (2002).
16. Suzuki, M., Furue, H. & Kobayashi, S. Polarizerless nanomaterial doped guest-host LCD exhibiting high luminance and good legibility. *Mol. Cryst. Liq. Cryst.* **368,** 191–196 (2001).
17. Kimura, M. *et al.* Self-organization of supramolecular complex composed of rigid dendritic porphyrin and fullerene. *J. Am. Chem. Soc.* **124,** 5274–5275 (2002).
18. Georgakilas, V. *et al.* Supramolecular self-asssembled fullerene nanostructures. *Proc. Natl Acad. Sci.* **99,** 5075–5080 (2002).
19. Sawamura, M., Iikura, H. & Nakamura, E. The first pentahaptofullerene metal complexes. *J. Am. Chem. Soc.* **118,** 12850–12851 (1996).
20. Tschierske, C. Non-conventional liquid crystals-the importance of micro-segregation for self-organization. *J. Mater. Chem.* **8,** 1485–1508 (1998).
21. Ruoff, R. S., Tse, D. S., Malhotra, R. & Lorents, D. C. Solubility of C_{60} in a variety of solvents. *J. Phys. Chem.* **97,** 3379–3383 (1993).
22. Iikura, H., Mori, S., Sawamura, M. & Nakamura, E. Endohedral homoconjugation in cyclopentadiene embedded in C_{60}. Theoretical and electrochemical evidence. *J. Org. Chem.* **62,** 7912–7913 (1997).
23. Sawamura, M., Kuninobu, Y. & Nakamura, E. Half-sandwich metallocene embedded in a spherically extended π-conjugate system. Synthesis, structure, and electrochemistry of $Rh(\eta^5\text{-}C_{60}Me_5)(CO)_2$. *J. Am. Chem. Soc.* **122,** 12407–12408 (2000).
24. Sawamura, M. *et al.* Hybrid of ferrocene and fullerene. *J. Am. Chem. Soc.* **124,** 9354–9355 (2002).
25. Manners, I. Putting metals into polymers. *Science* **294,** 1664–1666 (2001).

Supplementary Information accompanies the paper on *Nature*'s website (http://www.nature.com/nature).

Acknowledgements We thank Frontier Carbon Corporation for generous supply of C_{60}. The present research was supported by a Grant-in-Aid for Scientific Research (Specially Promoted Research) from the Ministry of Education, Culture, Sports, Science, and Technology.

Competing interests statement The authors declare that they have no competing financial interests.

Correspondence and requests for materials should be addressed to E.N. (e-mail: nakamura@chem.s.u-tokyo.ac.jp).

Re–Os isotopic evidence for long-lived heterogeneity and equilibration processes in the Earth's upper mantle

Anders Meibom*, Norman H. Sleep†, C. Page Chamberlain*, Robert G. Coleman*, Robert Frei‡, Michael T. Hren* & Joseph L. Wooden§

** Geological and Environmental Sciences, 320 Lomita Mall; and † Department of Geophysics, Mitchell Building, Stanford University, California 94305, USA*
‡ Geological Institute, University of Copenhagen, Øster Voldgade 10, DK-1350 Copenhagen K, Denmark
§ United States Geological Survey, 345 Middlefield Road, Menlo Park, California 94025, USA

The geochemical composition of the Earth's upper mantle[1–3] is thought to reflect 4.5 billion years of melt extraction, as well as the recycling of crustal materials. The fractionation of rhenium and osmium during partial melting in the upper mantle makes the Re–Os isotopic system well suited for tracing the extraction of melt and recycling of the resulting mid-ocean-ridge basalt[3]. Here we report osmium isotope compositions of more than 700 osmium-rich platinum-group element alloys derived from the upper mantle. The osmium isotopic data form a wide, essentially gaussian distribution, demonstrating that, with respect to Re–Os isotope systematics, the upper mantle is extremely heterogeneous. As depleted and enriched domains can apparently remain unequilibrated on a timescale of billions of years, effective equilibration seems to require high degrees of partial melting, such as occur under mid-ocean ridges or in back-arc settings, where percolating melts enhance the mobility of both osmium and rhenium. We infer that the gaussian shape of the osmium isotope distribution is the signature of a random mixing process between depleted and enriched domains, resulting from a 'plum pudding' distribution in the upper mantle, rather than from individual melt depletion events.

During partial melting in the upper mantle, Re is mildly incompatible, whereas Os is strongly compatible, resulting in high Re/Os elemental ratios in mid-ocean-ridge basalts (MORB) and correspondingly low Re/Os ratios in the depleted solid residue left behind[3]. As ^{187}Re decays to ^{187}Os with a half-life of about 42 billion years (Gyr) (ref. 4) the $^{187}Os/^{188}Os$ ratios of MORB and depleted mantle residue will diverge. The MORBs develop high, radiogenic $^{187}Os/^{188}Os$ ratios while the depleted mantle residues develop relatively low, unradiogenic $^{187}Os/^{188}Os$ ratios. When MORB is subducted back into the upper mantle re-equilibration with the depleted mantle residue is expected to take place, but the timescales and length scales on which this re-equilibration occurs are poorly constrained. One expectation has been that the present-day upper mantle would be characterized by a lower-than-chondritic $^{187}Os/^{188}Os$ ratio reflecting the time-averaged depletion in Re as a result of continuous extraction of MORB and preferential long-term storage of slabs of oceanic crust in the lower mantle. Estimates of the degree of slab isolation in the lower mantle vary widely, but are made with the assumption that the upper mantle is homogeneous with respect to its $^{187}Os/^{188}Os$ evolution[5–7]. However, mounting evidence indicates that $^{187}Os/^{188}Os$ heterogeneities can survive on long timescales in the upper mantle[8–12]. Examples include the discovery of ancient (0.8–1.2 Gyr) melt depletion events recorded in peridotite samples drilled from the young (~45 million years, Myr) Izu–Bonin–Mariana fore-arc subduction zone[9] and large variations among the subchondritic $^{187}Os/^{188}Os$ ratios measured in peridotite samples drilled from a single section of the